iScience

Article

Perivascular cerebrospinal fluid inflow matches interstitial fluid efflux in anesthetized rats

Graphical abstract

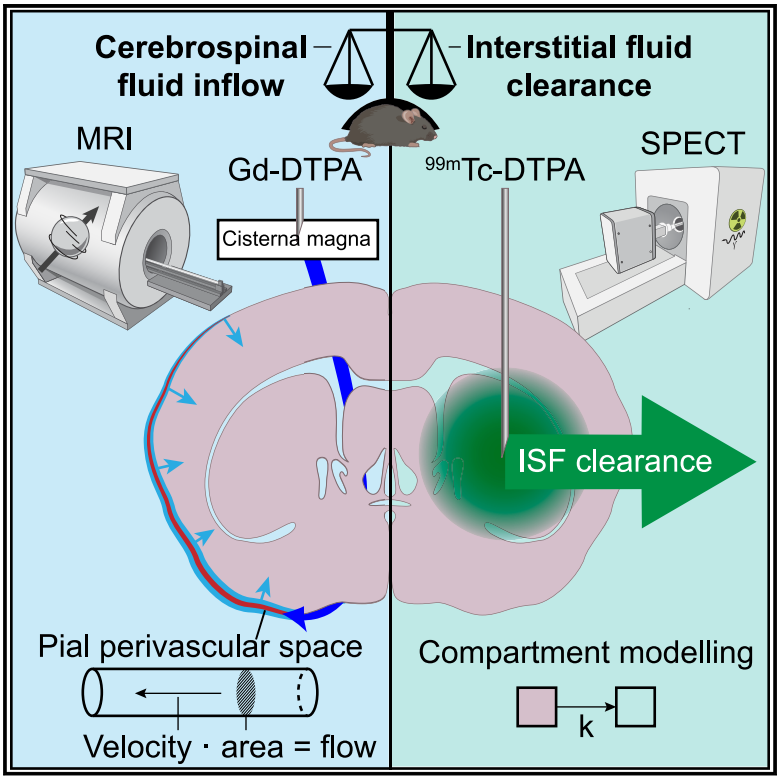

Highlights

- MRI with intrathecal contrast can quantify perivascular cerebrospinal fluid inflow
- Cerebrospinal fluid inflow matched interstitial fluid outflow in anesthetized rats
- Pial perivascular flow enters the neuropil rather than shunting to efflux routes
- Solute transport in pial perivascular spaces and inflow to neuropil are convective

Authors

Kristian N. Mortensen, Tuomas Lilius, Marko Rosenholm, Björn Sigurðsson, Douglas H. Kelley, Maiken Nedergaard

Correspondence

d.h.kelley@rochester.edu (D.H.K.), nedergaard@sund.ku.dk (M.N.)

In brief

Neuroscience; Techniques in neuroscience

Mortensen et al., 2025, iScience *28*, 112323
May 16, 2025
https://doi.org/10.1016/j.isci.2025.112323

CellPress

iScience

CellPress
OPEN ACCESS

Article

Perivascular cerebrospinal fluid inflow matches interstitial fluid efflux in anesthetized rats

Kristian N. Mortensen,[1,2] Tuomas Lilius,[1,3,4,5] Marko Rosenholm,[1] Björn Sigurðsson,[1] Douglas H. Kelley,[6,*] and Maiken Nedergaard[1,7,8,*]

[1]Center for Translational Neuromedicine, Faculty of Health and Medical Sciences, University of Copenhagen, Copenhagen, Denmark
[2]Danish Research Centre for Magnetic Resonance, Hvidovre Hospital, Hvidovre, Denmark
[3]Department of Pharmacology, Faculty of Medicine, University of Helsinki, Helsinki, Finland
[4]Individualized Drug Therapy Research Program, Faculty of Medicine, University of Helsinki, Helsinki, Finland
[5]Department of Emergency Medicine and Services, University of Helsinki and Helsinki University Hospital, Helsinki, Finland
[6]Department of Mechanical Engineering, University of Rochester, Rochester, NY, USA
[7]Center for Translational Neuromedicine, University of Rochester Medical Center, Rochester, NY, USA
[8]Lead contact
*Correspondence: d.h.kelley@rochester.edu (D.H.K.), nedergaard@sund.ku.dk (M.N.)
https://doi.org/10.1016/j.isci.2025.112323

SUMMARY

Waste solutes are cleared from the brain via outflow of interstitial fluid (ISF). Blood-brain barrier (BBB) water secretion and inflow of cerebrospinal fluid (CSF) via perivascular channels have been suggested as potential fluid sources to replace outflowing ISF. To assess the role of CSF inflow in brain clearance, we measured both CSF inflow and ISF outflow in ketamine/dexmedetomidine anesthetized rats. We used magnetic resonance imaging (MRI) and single-photon emission computed tomography (SPECT) to track tracer flows after infusion in CSF or ISF. CSF inflow was estimated at 0.5–0.7 $\mu L\ g^{-1}\ min^{-1}$ using either direct observation of perivascular flow or compartment modeling. ISF outflow was estimated at $0.47 \pm 0.05\ \mu L\ g^{-1}\ min^{-1}$ after intraparenchymal infusion. Our observations indicate that, under the anesthetic condition examined, inflowing CSF is sufficient to replace outflowing ISF, perivascular flow and CSF inflow to interstitium are dominated by convection, and diffusion and convection both contribute to tracer transport within the brain parenchyma.

INTRODUCTION

Maintaining a healthy microenvironment in the brain is essential for its function. Despite being metabolically highly active, the brain lacks a classical lymphatic system to remove metabolic waste. Instead, current evidence shows that waste solutes that cannot be metabolized in brain tissue or transported via the blood-brain barrier (BBB) are cleared along with interstitial fluid (ISF) via an extravascular route[1–3] before being collected by meningeal and extracranial lymphatic vessels.[4,5] Extravascular clearance of ISF has been estimated in anesthetized rodents to be on the order of 0.1–0.6 $\mu L\ g^{-1}\ min^{-1}$ calculated from the rate of elimination of injected inert tracers from brain tissue[6,7] and is highly depending on the anesthetic regimen.[8,9]

Several models have been proposed to explain the driving mechanism of ISF clearance (see study by Agarwal et al.[3] for a recent overview). The glymphatic model of brain clearance[10] proposes that ISF is cleared by bulk flow via venous perivascular spaces (PVSs) and along nerve roots and that this outflow is driven by a concomitant inflow to the interstitial space of cerebrospinal fluid (CSF) via arterial PVSs.[11,12] CSF is mainly produced by the choroid plexus in the ventricles and flows through cisterns, subarachnoid spaces, and PVSs that constitute a single continuous compartment. CSF moves along pial periarterial spaces in the direction of blood flow with speeds around 20 $\mu m\ s^{-1}$ in ketamine-xylazine or ketamine-medetomidine-anesthetized mice.[11,13–15] This pial perivascular flow follows the branching arteries and penetrating arterioles, supported by aquaporin-4 channels on the endfeet of astrocytes lining the PVS.

Several studies have demonstrated concomitant increases or decreases of CSF inflow and ISF clearance under different experimental conditions[15–20] in support of a model in which ISF outflow is supported by CSF inflow. The glymphatic model suggests a mass balance of inflowing CSF and cleared ISF, but we have found no studies comparing these in terms of quantitative volumetric flows.

Here, we quantitatively assessed the relationship between CSF inflow and ISF outflow in rats anesthetized with ketamine/dexmedetomidine. We used both compartment modeling techniques and direct observation of flow in large pial PVSs to estimate CSF inflow to the brain tissue and estimate the bulk outflow of ISF by measuring the elimination of a tracer from the interstitial space using single-photon-emission computed tomography (SPECT). The results demonstrate that under the anesthetic

conditions examined, inflow of CSF to the brain interstitium is sufficient to replace outflowing ISF, indicating that inflowing CSF constitutes a significant source of ISF and driver of its clearance in the anesthetized rat brain.

RESULTS

CSF tracer influx after intracisternal injection

To investigate the flow of CSF to brain parenchyma, we used T2-weighted (T2w) and quantitative dynamic contrast-enhanced MRI (DCE-MRI)[21] to measure the flow of a small paramagnetic tracer, gadopentetic acid (Gd-DTPA, 0.5 kDa; BioPAL, MA, USA) after infusion in the CSF in cisterna magna (12.5 mM, 40 μL, 2 μL min^{-1}) in healthy rats (n = 8, 200–300 g) anesthetized with ketamine-dexmedetomidine[9] (Figure 1A).

The tracer distribution pattern was similar to previous observations[22,23]: distribution through the subarachnoid space and PVSs of large surface arteries followed by distribution to the brain parenchyma (Figure 1B), preferentially along the pial periarterial spaces as has been recently demonstrated in humans.[24] In T2w images we observed parallel CSF-filled subarachnoid channels along the trunks of the pial arteries (Figure 1C). To avoid confusion with the gross subarachnoid space and with the PVSs of arteries and arterioles within the parenchyma, we here denote these parallel CSF-filled subarachnoid channels as pial PVSs. The pial PVSs served as the conduit for fast flow of tracer that followed the branching of the arteries before finally reaching the brain parenchyma where the tracer distributed. Within the brain parenchyma, tracer generally appeared to distribute to the tissue from a single source, i.e., a single pial PVS. Due to the convenient location of the middle cerebral artery (MCA) and the observation that its pial PVS was the single source of tracer for a well-defined region of the brain parenchyma, we decided to measure parenchymal CSF inflow of tracer arriving from the pial PVS of the trunk of MCA (Figure 1D). We measured CSF inflow (Q_{in}) as follows:

$$Q_{in} = \frac{\left|\vec{v}_{PVS}\right| \cdot A_{PVS}}{m_{territory}}, \qquad \text{(Equation 1)}$$

where $\left|\vec{v}_{PVS}\right|$ is the mean CSF flow velocity in the pial PVS, A_{PVS} is the cross-sectional area of the pial PVS, and $m_{territory}$ is the mass of the perfused territory.

To estimate the flow velocity, we measured the time-of-arrival of Gd-DTPA in the same segment of the MCA and estimated PVS flow velocity as the slope of the linear fit between distance and arrival-time of Gd-DTPA (Figure 1E). MCA pial PVS flow velocity, $\left|\vec{v}_{PVS}\right|$, was measured to be 0.95 ± 0.42 mm min^{-1} (Figure 1F).

To rule out that these results were biased by infusion of additional fluid or by diffusion of the flow tracer, we repeated the flow velocity measurement using a smaller volume infusion (10 μL, 2 μL min^{-1}) and a larger tracer molecule, Gadospin-P (200 kDa; BioPAL, MA, USA). These experiments resulted in a similar average PVS flow velocity in pial PVS of MCA of 1.01 ± 0.32 mm min^{-1} (n = 5).

To measure the pial PVS cross-sectional area, A_{PVS}, we used T2w images acquired with relatively long repetition and echo times (Figure 2A), which produced a high contrast between CSF and brain tissue. We applied bias-field correction to remove spatial signal inhomogeneity and converted the images to CSF volume fraction maps by assigning the signal intensity in cortex as 0 and signal intensity in the basal cistern as 1 (Figure 2B). We then measured the total pial PVS CSF volume in an 8 mm segment of the MCA trunk and calculated the average cross-sectional area as the volume divided by the length (Figure 2C). A_{PVS}, or average cross-sectional area of pial PVS was 0.082 ± 0.010 mm^2 (Figure 2D). To test the sensitivity of the cross-sectional area measurement to the choice of MRI imaging parameters, we repeated the measurement in a separate cohort using T2w-images acquired at a higher imaging resolution. The result was similar, albeit 15% lower: 0.069 ± 0.012 mm^2 (n = 12).

To determine the CSF perfusion territory of the MCA, we tracked the source of tracer for each voxel inside the brain parenchyma. We calculated a voxel-wise time-of-arrival map (Figure 3A), which allowed us to use a gradient-step algorithm to step toward voxels of earlier arrival time until reaching the subarachnoid space (see STAR Methods for details). We manually delineated the subarachnoid space territory of the MCA in each hemisphere (Figure 3B) using an average T2w MRI template.[25] If the gradient-step algorithm reached the delineated territory, the CSF source in the starting voxel was determined to be the MCA (Figure 3C). For some starting voxels the gradient-step algorithm did not terminate. Here, the CSF source was determined to be the same as the nearest starting voxel from which the gradient-step algorithm was successful. The $m_{territory}$, or average mass of the MCA PVS perfusion territory, was 0.157 ± 0.011 g (Figure 3D) assuming tissue density of 1.045 g ml^{-1}.[26]

Having acquired measurements of $\left|\vec{v}_{PVS}\right|$, A_{PVS}, and $m_{territory}$ for the pial PVS of MCA, we applied Equation 1 and found an average Q_{in} of 0.51 ± 0.25 μL g^{-1} min^{-1} (Figure 3E).

ISF clearance rate after intrastriatal injection

To estimate the rate of ISF clearance, we quantified the efflux rate of a tracer after intraparenchymal injection. To minimize tracer removal by diffusive transport to the brain surface, tracer was injected in deep tissue, i.e., striatum. In eight female rats (175–250 g), ^{99m}Tc-DTPA was infused through a chronically implanted cannula in striatum, and the distribution of the tracer was imaged using SPECT/CT for 220 min (Figure 4A). The intracranial compartment was manually segmented (Figure 4B), and the intracranial time-activity curve was corrected for infused activity and decay (Figure 4C). We calculated the efflux rate constant by fitting an exponential decay function to the data,[8,27] i.e.,

$$n_b(t) = n_i e^{-kt}, \qquad \text{(Equation 2)}$$

where $n_b(t)$ is the amount of tracer in the intracranial compartment at time t, n_i is the injected amount of tracer and k is the efflux rate constant (Figure 4D). Such decay is predicted by a compartment model in the absence of influx and is applicable once injection is complete. Assuming that the removal of tracer

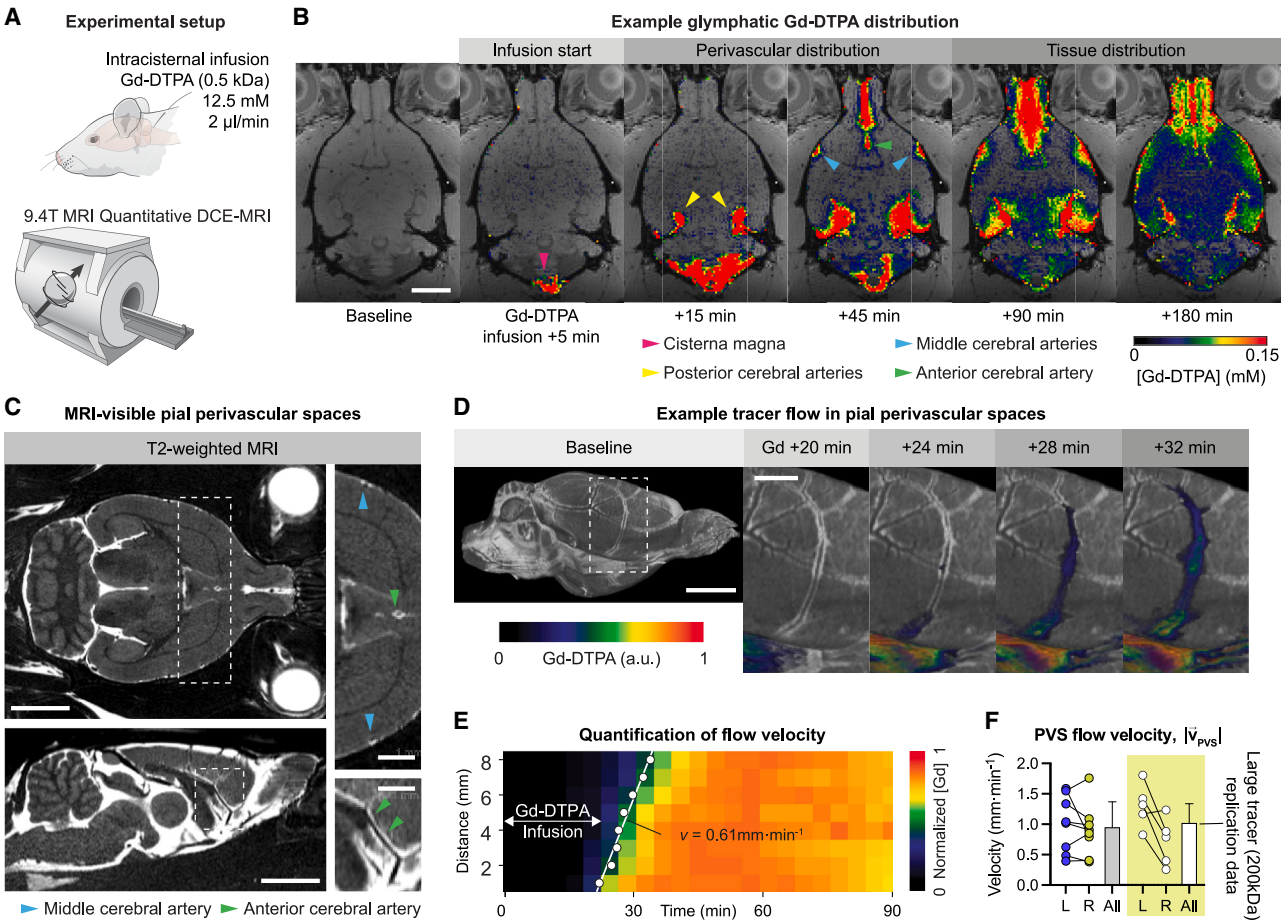

Figure 1. Dynamic contrast-enhanced MRI allows quantification of CSF flow velocity in pial perivascular spaces ($|\vec{v}_{PVS}|$)

(A) MRI was used to track the flow of a small paramagnetic tracer (Gd-DTPA) in CSF.

(B) After infusion in cisterna magna, glymphatic flow carried the tracer to the brain tissue via pial PVSs of major cerebral arteries. Scale bar: 5 mm.

(C) High-resolution T2-weighted images show parallel CSF-filled subarachnoid channels that served as conduits for the CSF flow. Scale bar: 5 mm, 2 mm in inserts.

(D) The front of the tracer wave arrived at the MCA ~20 min after the infusion started and covered the length of the trunk in ~10 min. Scale bar: 5 mm, 2 mm in inserts.

(E) We measured time-concentration-curves along the MCA and estimated the flow velocity as the slope of the linear fit of distance along the MCA and the time to exceed 20% of peak tracer concentration.

(F) Resulting flow velocity $|\vec{v}_{PVS}|$ (n = 8). We replicated the experiment using a larger tracer molecule and smaller infusion volume (n = 5, GadospinP, 200 kDa, 10 µL, 2 µL/min) with very similar results.

Abbreviations: CSF, cerebrospinal fluid; MCA, middle cerebral artery; MRI, magnetic resonance imaging. Data are represented as mean + standard deviation (STD).

compound measured by k occurs entirely by outflow of ISF, and that the concentration of the tracer in the outflow is equal to the concentration in the ISF, the ISF clearance rate is as follows[6,27]:

$$Q_{out} = k \cdot V_D, \qquad \text{(Equation 3)}$$

where V_D is the extracellular space volume per brain mass (approximately 200 µL/g brain tissue[28]). Thus, this clearance Q_{out} has units of volume per mass per time (e.g., µl g^{-1} min^{-1}). The efflux rate constant was on average 0.00235 ± 0.00026 min^{-1} (Figure 4E), which, assuming an extracellular space volume per brain mass of 200 µL/g, corresponds to an average Q_{out}, or ISF clearance rate, of 0.471 ± 0.053 µL g^{-1} min^{-1} (Figure 4F).

Pial perivascular fluid flow enters brain parenchyma

To test whether a significant amount of the pial PVS flow shunted or bypassed the brain parenchyma rather than entering the neuropil as CSF inflow, as has been suggested previously,[29] we compared the cumulative amount of tracer passing through the pial PVS with the amount of tracer accumulating in the

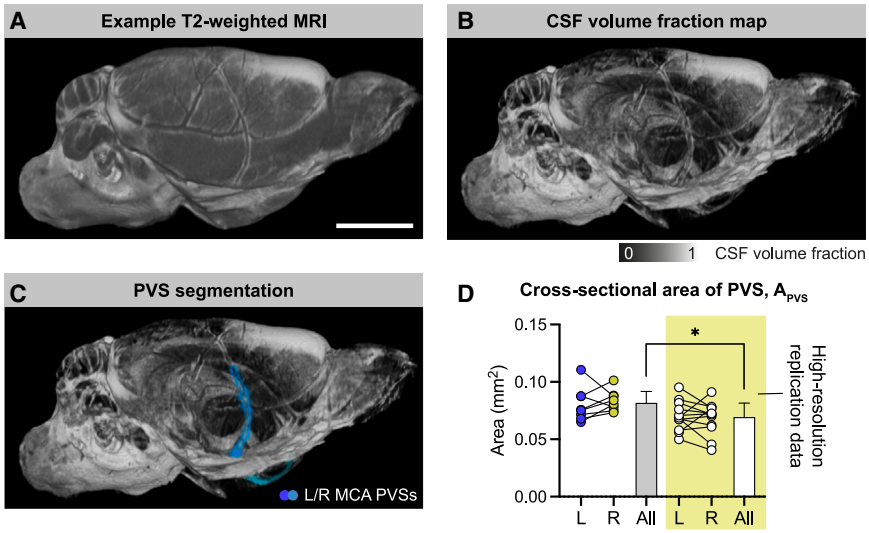

Figure 2. Calculation of cross-sectional area of the pial PVS (A_{PVS}) with high-resolution T2-weighted MRI

(A) T2-weighted MRI enabled measurement of the cross-sectional area of the PVS surrounding MCA. Scale bar: 5 mm.

(B) Example rendering of a parametric map of CSF volume fractions.

(C) The trunk of the MCA was manually segmented, and CSF partial volume maps were used to measure the cross-sectional area of the PVS.

(D) Resulting average cross-sectional area of the PVS surrounding MCA (A_{PVS}, n = 8). These calculations were repeated in a separate higher-resolution dataset (n = 12), producing a slightly but significantly lower estimate (p = 0.0249, unpaired two-tailed t test, t = 2.45, df = 18).

Abbreviations: CSF, cerebrospinal fluid; MCA, middle cerebral artery; MRI, magnetic resonance imaging; PVS, perivascular space. *: $p < 0.05$. Data are represented as mean + STD.

downstream brain tissue. We estimated the cumulative mass of tracer passing through the pial PVS as:

$$n_{PVS}(t) = \int_0^t c_{PVS}(t') \cdot |\vec{v}_{PVS}| \cdot A_{PVS}\, dt'. \qquad \text{(Equation 4)}$$

where $n_{PVS}(t)$ is the cumulative mass of tracer passing through the pial PVS, $c_{PVS}(t)$ is the concentration of tracer in the pial PVS and $|\vec{v}_{PVS}| \cdot A_{PVS}$ is the estimated average pial PVS flow.

To avoid partial-volume effects on the measurement of $c_{PVS}(t)$, we estimated it as the summed Gd-DTPA mass in a region of interest (ROI) covering the first 8 mm of the MCA divided by the sum of the T2w-derived CSF volume fractions in the ROI (Figure 5A).

Plotting $n_{PVS}(t)$ from the pial PVS of MCA along with $n_b(t)$ for the MCA territory of the brain parenchyma (Figure 5B), we observed that the two are nearly identical for the initial 60 min after infusion starts. Subsequently, tracer starts to clear from the brain parenchyma and $n_{PVS}(t)$ thus exceeds $n_b(t)$ (Figure 5C). To account for the clearance of tracer from the brain, we modeled the CSF inflow and ISF outflow using a simple kinetic model:

$$n_b(t) = \int_{t'=0}^{t} c_{in}(t') \cdot F_{in} - c_{out}(t') \cdot F_{out}\, dt', \qquad \text{(Equation 5)}$$

where $c_{in}(t)$ and $c_{out}(t)$ are the concentrations of tracer (nmol μl^{-1} or mM) in the inflow of CSF and the outflow of ISF, respectively, and F_{in} and F_{out} are the rates of CSF inflow to and ISF outflow from the interstitium, respectively (μl min^{-1}), both assumed to be independent of time (Figure 5D).

We applied Equation 5 to data from the MCA perfusion region. Since simple compartment models assume well-mixed compartments, we estimated that the tracer concentration in the outflowing ISF would equal the average ISF tracer concentration, i.e., the tracer content, $n_b(t)$, in the MCA perfusion territory, divided by the volume of ISF, or 20% of the tissue volume.[28] We assumed that only pial perivascular CSF flow contributed to tracer in the perfusion region and used c_{PVS} as input function. Equation 5 fitted the data well (Figure 5E) and F_{in} and F_{out} were estimated to be 0.085 ± 0.033 μL min^{-1} and 0.215 ± 0.080 μL min^{-1}, respectively (Figure 5F). The modeled F_{out} was thus more than 2-fold higher than F_{in} ($p < 0.001$). Accounting for the weight of the perfused territory, this corresponded to Q_{in} = 0.55 ± 0.23 μL g^{-1} min^{-1} and Q_{out} = 1.38 ± 0.58 μL g^{-1} min^{-1}. The model fit of F_{in} was highly correlated with the estimated value of $|\vec{v}_{PVS}| \cdot A_{PVS}$ calculated previously (Figure 5G) and regression analysis showed a near-unity relationship. Thus, our estimate of the fluid flow though the pial PVS corresponded well to the model-derived estimate of the fluid inflow from pial PVS into the brain tissue.

We additionally applied Equation 5 to estimate global inflow and outflow. We used the average concentration in pial PVSs and subarachnoid space surrounding the anterior, posterior, and middle cerebral arteries and circle of Willis as $c_{in}(t)$ and total brain tracer content, $n_b(t)$, divided by the total volume of ISF, which we assumed to be 20% of the total brain volume as $c_{out}(t)$ (Figures 5H and 5I). Again, the model fit the data well (Figure 5J), and F_{out} was 2-fold higher than F_{in} ($p < 0.0001$): F_{in} = 0.87 ± 0.22 μL min^{-1} and F_{out} = 1.72 ± 0.35 μL min^{-1}, respectively (Figure 5K). Accounting for the tissue weight, this corresponded to Q_{in} = 0.71 ± 0.21 μL g^{-1} min^{-1} and Q_{out} = 1.40 ± 0.31 μL g^{-1} min^{-1}. Plotting ISF clearance as a function of CSF perfusion (Figure 5L), we found Q_{in} and Q_{out} to be correlated and regression analysis found the relationship $Q_{out} = 1.07 \cdot Q_{in}$ + 0.64 μl g^{-1} min^{-1}.

DISCUSSION

The glymphatic model proposes that inflow of "clean" CSF (Q_{in}) though PVSs to the brain parenchyma drives a concomitant outflow of "dirty" ISF (Q_{out}) thereby clearing the brain interstitial space of metabolic waste.[10] If CSF inflow is

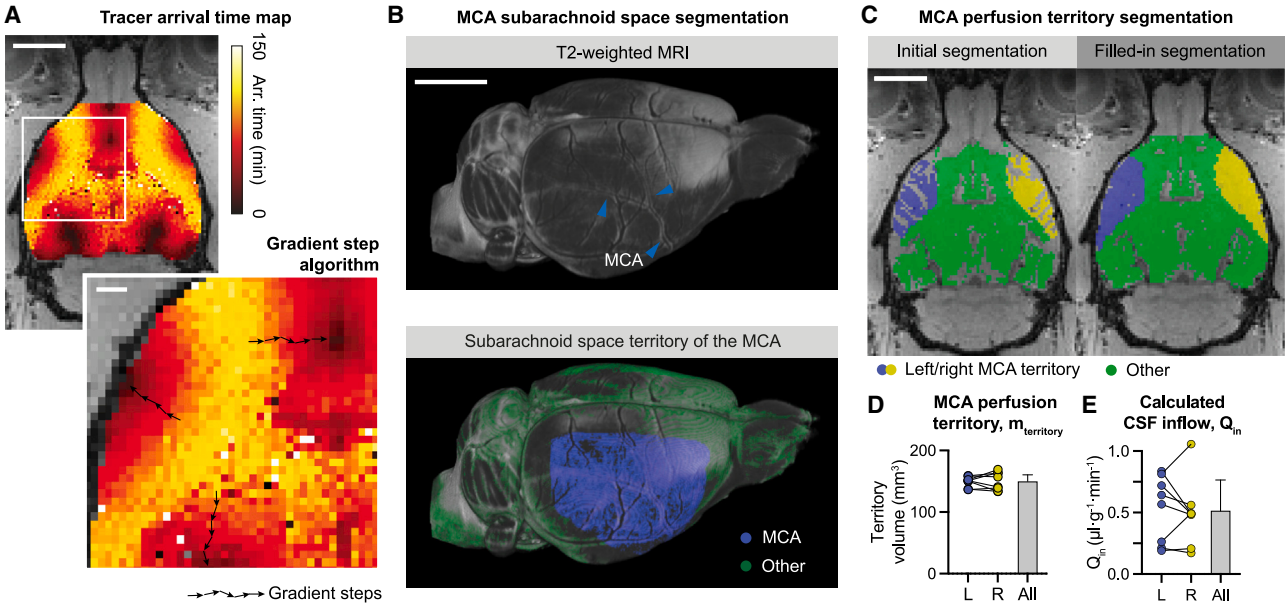

Figure 3. Calculation of the CSF perfusion territory of MCA ($m_{territory}$) and CSF inflow (Q_{in})

(A) We calculated a tracer arrival time map and used a gradient step algorithm to estimate whether the tracer source for each voxel was the MCA PVS or not. Scale bar: 5 mm, 1 mm in inserts.

(B) To estimate the perfusion territory of MCA, we segmented the PVS and subarachnoid space in the surface region of the MCA. Scale bar: 5 mm.

(C) Voxels for which the tracer source was not identified automatically were matched to the nearest neighbor. Scale bar: 5 mm.

(D) The resulting volume of the MCA perfusion territory ($m_{territory}$, n = 8).

(E) Applying Equation 1 to data from Figures 1, 2, and 3 resulted in a measurement of the CSF inflow to brain tissue (Q_{in}).

Abbreviations: CSF, cerebrospinal fluid; MCA, middle cerebral artery; MRI, magnetic resonance imaging; PVS, perivascular space. Data are represented as mean + STD.

the sole driver of ISF outflow and thus source of new ISF, Q_{in} should equal or exceed Q_{out}, and the lack of concurrent measurements of the two parameters has been raised as critique of the glymphatic model.[1] Our quantitative estimates in rats under ketamine/dexmedetomidine anesthesia of Q_{in} and Q_{out} closely match, suggesting that under these conditions, CSF inflow is sufficient to replace outflowing ISF and is a feasible source of new ISF. We additionally found the flux of tracer in the pial PVS to closely match the delivery of tracer into brain tissue. This demonstrates that pial perivascular CSF flows antegrade with the blood flow and enters brain parenchyma where it mixes with ISF, rather than bypassing brain tissue as has been suggested.[29]

In peripheral tissues, metabolic waste is cleared by the lymphatic system. Lymph flow rates appear to follow metabolic demand, e.g., extravasation of tracer albumin is higher in heart tissue than in skeletal muscle[30] and clearance of intramuscular injected human serum albumin is lower in resting than in active skeletal muscle.[31] Assuming purely convective extravasation of tracer albumin following the Starling principle, an upper limit of lymph flow from rat heart muscle was estimated at 0.45–0.48 µL g^{-1} min^{-1} compared to 0.035–0.1 µL g^{-1} min^{-1} in skeletal muscle.[32] Thus, the present estimate of cerebral ISF clearance of 0.47 ± 0.05 µL g^{-1} min^{-1} is consistent with other high-metabolic tissues, further indicating that CSF inflow of 0.5–0.7 µL g^{-1} min^{-1} could be sufficient to clear brain tissue of metabolic waste.

The ionic compositions of ISF and CSF are very similar[33] making CSF a suitable medium to replace ISF. CSF is mainly produced at the choroid plexuses in the cerebral ventricles. Estimates of total CSF production in rats depend on the choice of measurement method, from ~1.7 µL g^{-1} min^{-1} using a tracer dilution method[34,35] to ~0.7 µL g^{-1} min^{-1} by direct observation of production in the lateral and third ventricles.[36] Thus, if all CSF theoretically enters the PVSs, it would be sufficient to account for all glymphatic flow. However, neither of these calculations takes into account that CSF production and glymphatic flow vary with the sleep-wake cycle.[17,37] Most tracer studies have shown that only 20%–30% of CSF enters the PVS, while the remaining CSF flows down along spinal cord or is shunted out directly to peripheral tissues via the meningeal/cervical lymphatics.[21,23]

Another feasible source of fluid for ISF production is net water flow across the BBB. Currently, no method exists to estimate the total net water movement across the BBB.[38] Rather, only unidirectional water transport from blood plasma to the brain tissue can be estimated using tritiated water as a tracer (sec. 2.1 in a study by Hladky and Barrand[39]), or using diffusion-weighted arterial spin labeling MRI,[40] showing that a majority (70%–90%) of water molecules cross from plasma to brain tissue in a single pass, or roughly 200–500 µL g^{-1} min^{-1} depending on brain mass and perfusion, exceeding CSF inflow by several orders of magnitude. Ostensibly, an equal flow exists in the reverse direction, from the brain tissue to blood plasma, but a small

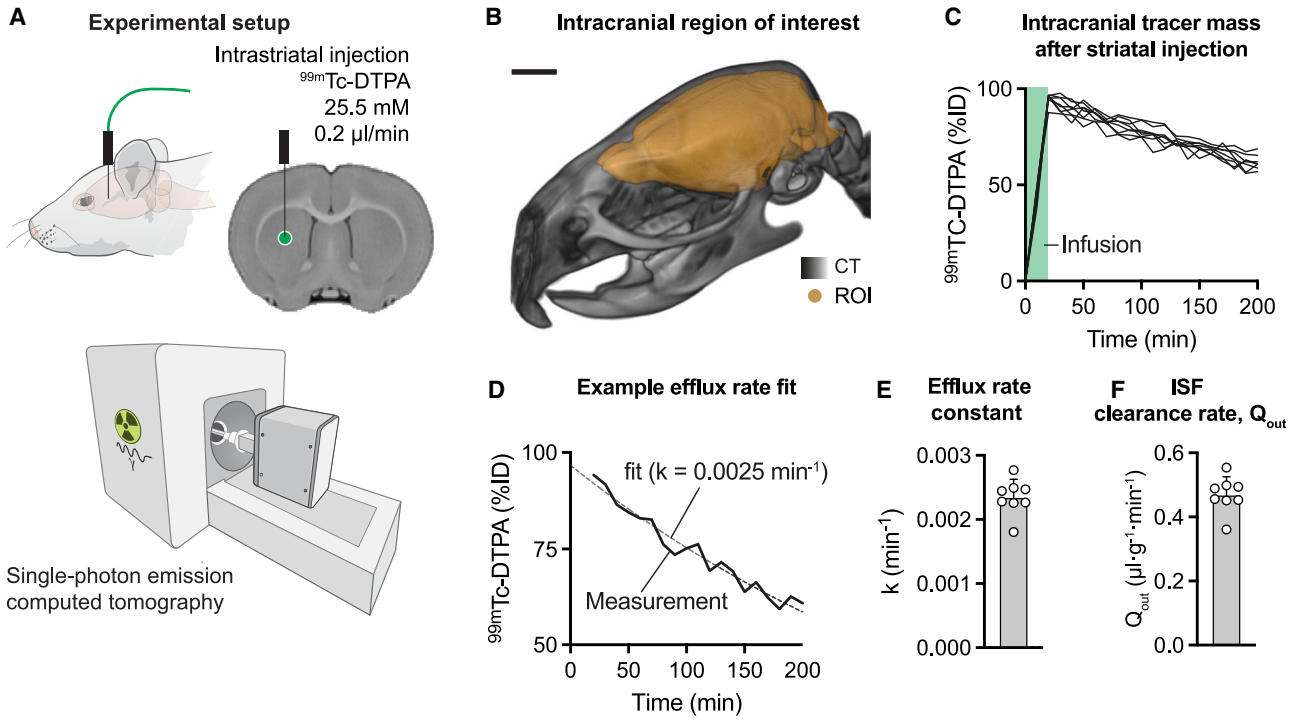

Figure 4. Calculation of ISF clearance from deep brain tissue

(A) Single-photon emission computed tomography (SPECT) was used to track the clearance of a small radiotracer (^{99m}Tc-DTPA) from interstitial fluid after infusion injection in deep brain tissue.

(B) The intracranial region of interest was drawn using reference CT. Scale bar: 5 mm.

(C) Residual ^{99m}Tc-DTPA normalized to the injected dose (%ID) in the intracranial compartment after infusion in the striatum from individual rats.

(D) Example result of the fitting routine to measure the efflux rate constant, k.

(E and F) The ISF clearance rate was calculated by multiplying k with the ISF volume per brain weight.

Abbreviations: DTPA, diethylene-triamine-pentaacetate; ISF, interstitial fluid. Data are represented as mean + STD.

discrepancy between blood-to-ISF and ISF-to-blood water transport could give rise to a net inflow.

It has been suggested that ISF-to-CSF transport could account for ~10% of extravascular brain clearance,[7,27] potentially causing cleared metabolic waste to reenter brain tissue from CSF. Studies of microspheres flowing in the pial PVS of the MCA[11,14] have observed only flow in the same direction as blood flow, with no indication reverse flow. While some local recirculation from ISF to perivascular CSF at the arteriolar or capillary level is feasible, this is be downstream of the present observations and does not affect the results.

We quantified CSF inflow using DCE-MRI after cisterna magna tracer infusion, the results of which matched ISF outflow measured by SPECT after intrastriatal tracer injection. Reanalyzing the DCE-MRI data using compartment modeling to allow estimation of both CSF inflow and ISF outflow yielded very similar results for inflow, but a 2-fold higher ISF outflow estimate. This model implicitly assumes the compartments to be well mixed, i.e., that the tracer concentration in ISF cleared from the brain tissue equals the average concentration within the compartment. This assumption is clearly violated as seen in Figure 1B and Figure 3A, and by direct transport of tracer to the subarachnoid or perivenous space shortly after entering the brain. Conversely, intrastriatal injection introduces tracer locally and far from the brain surface, where diffusive transport directly to the subarachnoid or perivenous spaces can have less effect in its clearance from brain tissue. CSF inflow and ISF clearance should optimally be measured from the same tissue. We chose to inject tracer in the striatum to avoid direct diffusive transport to subarachnoid or perivenous spaces and because of its similarity in cerebral blood flow and metabolism under similar anesthetic regimens.[41] For these reasons, we believe the estimate from intrastriatal injection is a better measure of ISF outflow than is the estimate from cisterna magna infusion. Alternatively, a net fluid inflow could provide an explanation of the intercept of ~0.6 µL g^{-1} min^{-1} in the regression of globally modeled outflow to inflow (Figure 5L).

The CSF inflow quantification method presented here is to our knowledge the first to measure perfusion of the brain tissue in units of flow per tissue weight (here µl g^{-1} min^{-1}). This unit is convenient because it allows for direct comparison between organs, between subjects, and between species. In mice, a detailed study[42] of CSF influx in individual PVSs estimated the brain-wide perfusion rate to be 0.625 µL g^{-1} min^{-1}, agreeing closely with an earlier approximation for mice[43] (0.5 µL g^{-1} min^{-1}) and with our estimate for rats (0.5 µL g^{-1} min^{-1}). Notably, if human brain tissue is perfused at the same rate we measured, the ~1.4 kg mass of a human brain would imply CSF influx at a

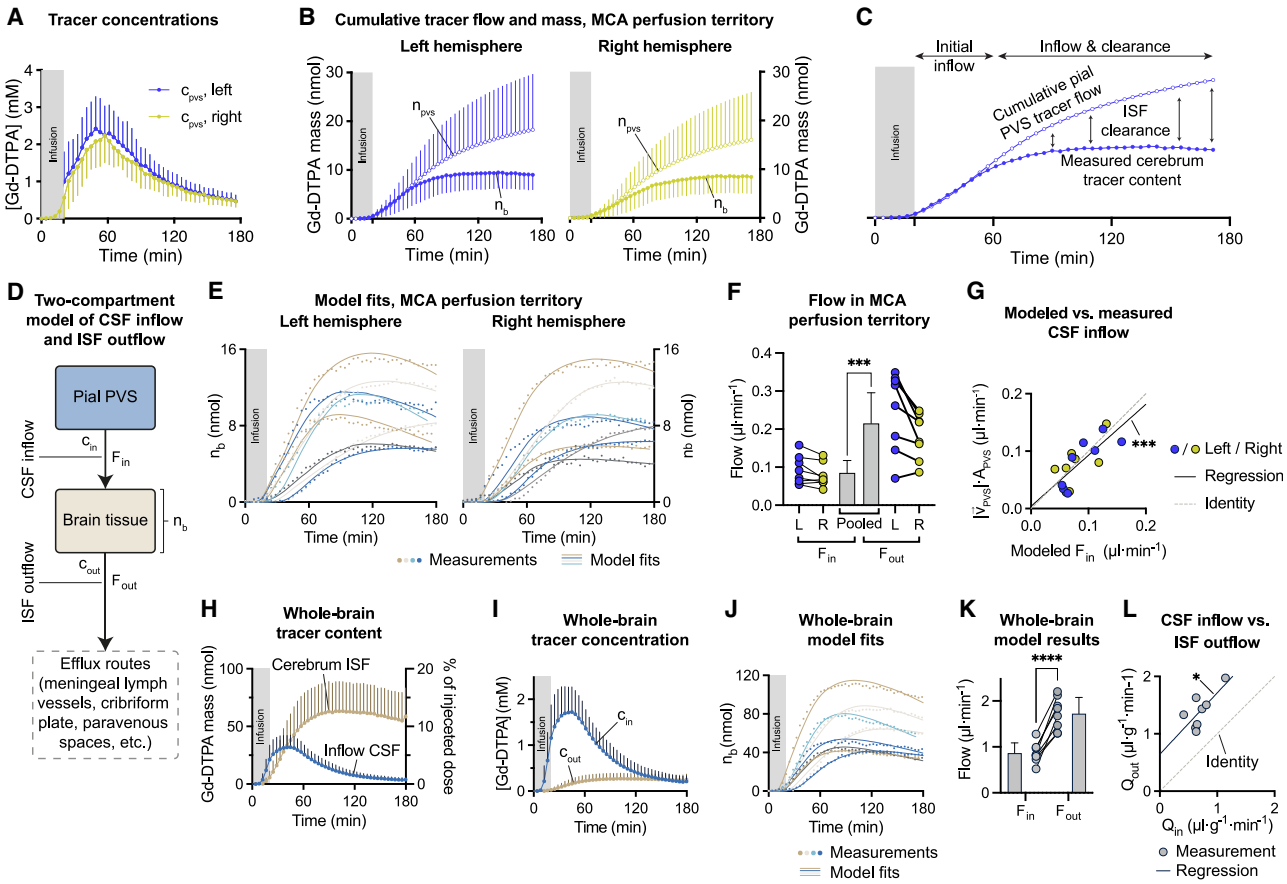

Figure 5. Modeling shows that pial perivascular tracer flow enters the brain parenchyma

(A) Estimated pial PVS tracer concentration.

(B) Integrated pial PVS tracer flow (n_{PVS}) plotted against measured brain tracer mass (n_b).

(C) n_{PVS} diverges from n_b 60 min after infusion when tracer starts to clear from the brain parenchyma.

(D) Compartment model to account for both tracer inflow and clearance to and from the brain parenchyma.

(E and F) Compartment model fits and results for MCA perfusion territory show lower estimates of F_{in} than F_{out} ($p = 0.00087$, paired two-tailed t test, t = 5.53, df = 7, $n = 8$).

(G) Modeled parenchymal CSF inflow correlated well with estimated CSF flow in pial PVS for the MCA perfusion territory. ($p = 0.00066$, linear regression, y = 0.89x + 0.004x, df = 14, $R^2 = 0.58$, each replicate represents a per-hemisphere measurement, i.e., $n = 16$).

(H and I) Estimated tracer mass and concentration in whole-brain ISF and CSF in inflow pathways.

(J and K) Whole-brain compartment model fits and results replicate findings of lower F_{in} than F_{out} in MCA perfusion territory ($p = 0.000038$, paired two-tailed t test, t = 9.15, df = 7, $n = 8$).

(L) Whole-brain model fits of ISF clearance and CSF perfusion showed a linear relationship with a high intercept ($p = 0.04$, linear regression, y = 1.07x + 0.64, df = 6, $n = 8$).

Abbreviations: CSF, cerebrospinal fluid; ISF, interstitial fluid; MCA, middle cerebral artery; PVS, perivascular space. *: $p < 0.05$, ***$p < 0.001$, ****$p < 0.0001$. Data are represented as mean + STD.

rate of ~1 L/day, notably of the same order of magnitude as the typically measured CSF production of ~0.5 L/day.[44] Since per-gram rates of both CSF production[38] and cerebral metabolism[45] in rat brain tissue exceed those of human brain tissue by a factor of 2–4, the direct extrapolation of CSF influx rates to human could overestimate true CSF influx by as much, so an adjusted estimate might lie still closer to the measured production rate.

Our methods could potentially be applied to human DCE-MRI after intrathecal tracer injection, which is feasible in humans, albeit rarely performed in healthy subjects due to the invasiveness. A recent analysis[24] of human DCE-MRI after intrathecal injection in awake subject showed that tracer appeared at the M1 segment of MCA ~40 min before appearing at the M3 segment. The distance from M1 to M3 segments of MCA is approximately 5 cm, giving a first order estimate of the flow velocity of 1.25 mm min^{-1}. Velocities in that range are feasible to measure using phase-contrast MRI[46,47] albeit the measurement is complicated by the fact that brain tissue displaces 0.02–0.5 mm with every cardiac pulsation in humans.[48] Due to the different species and brain states, these measurements are not comparable to ours but demonstrate the feasibility of quantifying human CSF inflow to brain tissue.

This quantitative study shows that CSF inflow in young rats anesthetized with ketamine/dexmedetomidine is in the range 0.5–0.7 $\mu L\ g^{-1}\ min^{-1}$, whereas ISF outflow is estimated at $0.47 \pm 0.05\ \mu L\ g^{-1}\ min^{-1}$. Our analysis suggests that CSF inflow can match fluid efflux and is thus a significant source of fluid to replace ISF cleared by glymphatic efflux. This finding underscores the importance of the age-dependent decline in CSF production as well as in glymphatic flow,[17,31] and further illustrates why aging is the most important risk factor for proteinopathies and dementia.[49] Refined versions of the imaging and analysis tools presented here may in the future provide biomarkers for clinical assessment of glymphatic flow.

Limitations of the study

This study provides the first estimates of CSF inflow and ISF clearance under the same experimental conditions, indicating a link between the two. The measurements are subject to high uncertainty due to both biological and measurement variation, e.g., measuring the cross-sectional area of the pial PVS in the higher-resolution dataset resulted in a 15% reduction (Figure 2D). To avoid direct diffusive transport out of brain tissue, ISF clearance was measured after infusion in striatum, while CSF inflow was measured in cortical tissue. One study has showed that there is a region difference in ISF clearance of 35% between caudate nucleus and midbrain.[50] Further study is warranted to validate the link between CSF inflow and ISF clearance under different experimental conditions and in other species.

RESOURCE AVAILABILITY

Lead contact

Requests for further information and resources should be directed to and will be fulfilled by the lead contact, Maiken Nedergaard (nedergaard@sund.ku.dk).

Materials availability

This study did not generate new unique reagents.

Data and code availability

- Unprocessed MRI data have been deposited at Mendeley Data and are publicly available as of the date of publication at Mendeley Data: https://doi.org/10.17632/78rvmj2wh8.1.
- All original code has been deposited at Mendeley Data and is publicly available as of the date of publication at Mendeley Data: https://doi.org/10.17632/78rvmj2wh8.1.
- Any additional information required to reanalyze the data reported in this paper is available from the lead contact upon request.
- For SPECT data presented in Figure 4, we refer to the originating paper.[51]

ACKNOWLEDGMENTS

The work was supported by grants from the Lundbeck Foundation (R249-2017-1511, K.N.M. and R386-2021-165, M.N.), the Novo Nordisk Foundation (NNF20OC0066419, M.N.), Danmarks Frie Forskningsfond (3101-00282B, M.N.), the U.S. Army (MURIW911NF1910280, M.N. and D.H.K.), the National Institutes of Health (R01A 012707 and AT011439 M.N.), the NIH BRAIN Initiative (U19NS128613, M.N. and D.H.K.), the NIH National Center for Complementary and Integrative Health (R01AT012312, D.H.K. and M.N.), the Dr. Miriam and Sheldon G. Adelson Medical Research Foundation (M.N.), The Simons Foundation (811237, M.N.), the Cure Alzheimer's Fund (M.N.), the Hunam Frontiers Science Program (RGP0036, M.N.), and JPND (1098-0030B and 2092-00006, M.N.).

AUTHOR CONTRIBUTIONS

K.N.M., D.H.K., and M.N. were responsible for experimental design. K.N.M., T.L., B.S., and M.R. were responsible for data collection. K.N.M. and D.H.K. were responsible for data analysis. K.N.M. was responsible for figure preparation. K.N.M., D.H.K., and M.N. were responsible for manuscript writing and preparation. All authors have read and have approved the final version of this manuscript.

DECLARATION OF INTERESTS

The authors declare no competing interests.

STAR★METHODS

Detailed methods are provided in the online version of this paper and include the following:

- KEY RESOURCES TABLE
- EXPERIMENTAL MODEL AND STUDY PARTICIPANTS DETAILS
- METHOD DETAILS
  - Cisterna magna cannulation
  - Mechanical ventilation
  - MRI experiments
  - PVS distance measurements
  - PVS cross-sectional area estimation
  - Velocity estimation
  - MCA CSF perfusion volume estimation
  - SPECT imaging
  - SPECT/CT analysis
- QUANTIFICATION AND STATISTICAL ANALYSIS

Received: September 26, 2024
Revised: November 27, 2024
Accepted: March 26, 2025
Published: March 30, 2025

REFERENCES

1. Hladky, S.B., and Barrand, M.A. (2022). The glymphatic hypothesis: the theory and the evidence. Fluids Barriers CNS *19*, 9.
2. Bohr, T., Hjorth, P.G., Holst, S.C., Hrabětová, S., Kiviniemi, V., Lilius, T., Lundgaard, I., Mardal, K.A., Martens, E.A., Mori, Y., et al. (2022). The glymphatic system: Current understanding and modeling. iScience *25*, 104987.
3. Agarwal, N., Lewis, L.D., Hirschler, L., Rivera, L.R., Naganawa, S., Levendovszky, S.R., Ringstad, G., Klarica, M., Wardlaw, J., Iadecola, C., et al. (2024). Current Understanding of the Anatomy, Physiology, and Magnetic Resonance Imaging of Neurofluids: Update From the 2022 "ISMRM Imaging Neurofluids Study group" Workshop in Rome. J. Magn. Reson. Imag. *59*, 431–449. https://doi.org/10.1002/jmri.28759.
4. Da Mesquita, S., Louveau, A., Vaccari, A., Smirnov, I., Cornelison, R.C., Kingsmore, K.M., Contarino, C., Onengut-Gumuscu, S., Farber, E., Raper, D., et al. (2018). Functional aspects of meningeal lymphatics in ageing and Alzheimer's disease. Nature *560*, 185–191.
5. Louveau, A., Plog, B.A., Antila, S., Alitalo, K., Nedergaard, M., and Kipnis, J. (2017). Understanding the functions and relationships of the glymphatic system and meningeal lymphatics. J. Clin. Investig. *127*, 3210–3219.
6. Hladky, S.B., and Barrand, M.A. (2018). Elimination of substances from the brain parenchyma: efflux via perivascular pathways and via the blood–brain barrier. Fluids Barriers CNS *15*, 30.
7. Abbott, N.J. (2004). Evidence for bulk flow of brain interstitial fluid: significance for physiology and pathology. Neurochem. Int. *45*, 545–552.
8. Groothuis, D.R., Vavra, M.W., Schlageter, K.E., Kang, E.W.Y., Itskovich, A.C., Hertzler, S., Allen, C.V., and Lipton, H.L. (2007). Efflux of Drugs and Solutes from Brain: The Interactive Roles of Diffusional Transcapillary

Transport, Bulk Flow and Capillary Transporters. J. Cerebr. Blood Flow Metabol. *27*, 43–56.

9. Persson, N.D.Å., Lohela, T.J., Mortensen, K.N., Rosenholm, M., Li, Q., Weikop, P., Nedergaard, M., and Lilius, T.O. (2024). Anesthesia Blunts Carbon Dioxide Effects on Glymphatic Cerebrospinal Fluid Dynamics in Mechanically Ventilated Rats. Anesthesiology *141*, 338–352.
10. Iliff, J.J., Wang, M., Liao, Y., Plogg, B.A., Peng, W., Gundersen, G.A., Benveniste, H., Vates, G.E., Deane, R., Goldman, S.A., et al. (2012). A Paravascular Pathway Facilitates CSF Flow Through the Brain Parenchyma and the Clearance of Interstitial Solutes, Including Amyloid β. Sci. Transl. Med. *4*, 147ra111.
11. Mestre, H., Tithof, J., Du, T., Song, W., Peng, W., Sweeney, A.M., Olveda, G., Thomas, J.H., Nedergaard, M., and Kelley, D.H. (2018). Flow of cerebrospinal fluid is driven by arterial pulsations and is reduced in hypertension. Nat. Commun. *9*, 4878.
12. Iliff, J.J., Wang, M., Zeppenfeld, D.M., Venkataraman, A., Plog, B.A., Liao, Y., Deane, R., and Nedergaard, M. (2013). Cerebral Arterial Pulsation Drives Paravascular CSF–Interstitial Fluid Exchange in the Murine Brain. J. Neurosci. *33*, 18190–18199.
13. Bedussi, B., Almasian, M., Vos, J. de, VanBavel, E., and Bakker, E.N. (2017). Paravascular spaces at the brain surface: Low resistance pathways for cerebrospinal fluid flow. J. Cerebr. Blood Flow Metabol. *38*, 719–726.
14. Raghunandan, A., Ladron-de-Guevara, A., Tithof, J., Mestre, H., Du, T., Nedergaard, M., Thomas, J.H., and Kelley, D.H. (2021). Bulk flow of cerebrospinal fluid observed in periarterial spaces is not an artifact of injection. Elife *10*, e65958.
15. Holstein-Rønsbo, S., Gan, Y., Giannetto, M.J., Rasmussen, M.K., Sigurdsson, B., Beinlich, F.R.M., Rose, L., Untiet, V., Hablitz, L.M., Kelley, D.H., and Nedergaard, M. (2023). Glymphatic influx and clearance are accelerated by neurovascular coupling. Nat. Neurosci. *26*, 1042–1053.
16. Peng, W., Achariyar, T.M., Li, B., Liao, Y., Mestre, H., Hitomi, E., Regan, S., Kasper, T., Peng, S., Ding, F., et al. (2016). Suppression of glymphatic fluid transport in a mouse model of Alzheimer's disease. Neurobiol. Dis. *93*, 215–225.
17. Xie, L., Kang, H., Xu, Q., Chen, M.J., Liao, Y., Thiyagarajan, M., O'Donnell, J., Christensen, D.J., Nicholson, C., Iliff, J.J., et al. (2013). Sleep Drives Metabolite Clearance from the Adult Brain. Science *342*, 373–377.
18. Kress, B.T., Iliff, J.J., Xia, M., Wang, M., Wei, H.S., Zeppenfeld, D., Xie, L., Kang, H., Xu, Q., Liew, J.A., et al. (2014). Impairment of paravascular clearance pathways in the aging brain. Ann. Neurol. *76*, 845–861.
19. Iliff, J.J., Chen, M.J., Plog, B.A., Zeppenfeld, D.M., Soltero, M., Yang, L., Singh, I., Deane, R., and Nedergaard, M. (2014). Impairment of Glymphatic Pathway Function Promotes Tau Pathology after Traumatic Brain Injury. J. Neurosci. *34*, 16180–16193.
20. Jiang-Xie, L.-F., Drieu, A., Bhasiin, K., Quintero, D., Smirnov, I., and Kipnis, J. (2024). Neuronal dynamics direct cerebrospinal fluid perfusion and brain clearance. Nature *627*, 157–164.
21. Lee, H., Mortensen, K., Sanggaard, S., Koch, P., Brunner, H., Quistorff, B., Nedergaard, M., and Benveniste, H. (2018). Quantitative Gd-DOTA uptake from cerebrospinal fluid into rat brain using 3D VFA-SPGR at 9.4T. Magn. Reson. Med. *79*, 1568–1578.
22. Iliff, J.J., Lee, H., Yu, M., Feng, T., Logan, J., Nedergaard, M., and Benveniste, H. (2013). Brain-wide pathway for waste clearance captured by contrast-enhanced MRI. J. Clin. Investig. *123*, 1299–1309.
23. Mortensen, K.N., Sanggaard, S., Mestre, H., Lee, H., Kostrikov, S., Xavier, A.L.R., Gjedde, A., Benveniste, H., and Nedergaard, M. (2019). Impaired Glymphatic Transport in Spontaneously Hypertensive Rats. J. Neurosci. *39*, 6365–6377.
24. Eide, P.K., and Ringstad, G. (2024). Functional analysis of the human perivascular subarachnoid space. Nat. Commun. *15*, 2001.
25. Lilius, T.O., Mortensen, K.N., Deville, C., Lohela, T.J., Stæger, F.F., Sigurdsson, B., Fiordaliso, E.M., Rosenholm, M., Kamphuis, C., Beekman, F.J., et al. (2023). Glymphatic-assisted perivascular brain delivery of intrathecal small gold nanoparticles. J. Contr. Release *355*, 135–148.
26. DiResta, G.R., Lee, J.B., and Arbit, E. (1991). Measurement of brain tissue specific gravity using pycnometry. J. Neurosci. Methods *39*, 245–251.
27. Cserr, H.F., Cooper, D.N., Suri, P.K., and Patlak, C.S. (1981). Efflux of radiolabeled polyethylene glycols and albumin from rat brain. Am. J. Physiol. *240*, F319–F328.
28. Syková, E., and Nicholson, C. (2008). Diffusion in Brain Extracellular Space. Physiol. Rev. *88*, 1277–1340.
29. Ma, Q., Ries, M., Decker, Y., Müller, A., Riner, C., Bücker, A., Fassbender, K., Detmar, M., and Proulx, S.T. (2019). Rapid lymphatic efflux limits cerebrospinal fluid flow to the brain. Acta Neuropathol. *137*, 151–165.
30. Renkin, E.M., Joyner, W.L., Gustafson-Sgro, M., Plopper, G., and Sibley, L. (1989). Albumin extravasation rates in tissues of anesthetized and unanesthetized rats. J. Appl. Physiol. *66*, 2056–2060.
31. Havas, E., Parviainen, T., Vuorela, J., Toivanen, J., Nikula, T., and Vihko, V. (1997). Lymph flow dynamics in exercising human skeletal muscle as detected by scintography. J. Physiol. *504*, 233–239.
32. Renkin, E.M., and Wiig, H. (1994). Limits to Steady-State Lymph Flow Rates Derived from Plasma-to-Tissue Uptake Measurements. Microvasc. Res. *47*, 318–328.
33. Thrane, A.S., Rangroo Thrane, V., and Nedergaard, M. (2014). Drowning stars: reassessing the role of astrocytes in brain edema. Trends Neurosci. *37*, 620–628.
34. Pullen, R.G., DePasquale, M., and Cserr, H.F. (1987). Bulk flow of cerebrospinal fluid into brain in response to acute hyperosmolality. Am. J. Physiol. *253*, F538–F545.
35. Chodobski, A., Szmydynger-Chodobska, J., and Johanson, C.E. (1998). Vasopressin mediates the inhibitory effect of central angiotensin II on cerebrospinal fluid formation. Eur. J. Pharmacol. *347*, 205–209.
36. Karimy, J.K., Kahle, K.T., Kurland, D.B., Yu, E., Gerzanich, V., and Simard, J.M. (2015). A novel method to study cerebrospinal fluid dynamics in rats. J. Neurosci. Methods *241*, 78–84.
37. Liu, G., Mestre, H., Sweeney, A.M., Sun, Q., Weikop, P., Du, T., and Nedergaard, M. (2020). Direct Measurement of Cerebrospinal Fluid Production in Mice. Cell Rep. *33*, 108524.
38. MacAulay, N. (2021). Molecular mechanisms of brain water transport. Nat. Rev. Neurosci. *22*, 326–344.
39. Hladky, S.B., and Barrand, M.A. (2016). Fluid and ion transfer across the blood–brain and blood–cerebrospinal fluid barriers; a comparative account of mechanisms and roles. Fluids Barriers CNS *13*, 19.
40. Lawrence, K.S.S., Owen, D., and Wang, D.J.J. (2012). A Two-Stage Approach for Measuring Vascular Water Exchange and Arterial Transit Time by Diffusion-Weighted Perfusion MRI, *67*, pp. 1275–1284.
41. Xu, M., Bo, B., Pei, M., Chen, Y., Shu, C.Y., Qin, Q., Hirschler, L., Warnking, J.M., Barbier, E.L., Wei, Z., et al. (2022). High-resolution relaxometry-based calibrated fMRI in murine brain: Metabolic differences between awake and anesthetized states. J. Cerebr. Blood Flow Metabol. *42*, 811–825.
42. Boster, K.A.S., Cai, S., Ladrón-de-Guevara, A., Sun, J., Zheng, X., Du, T., Thomas, J.H., Nedergaard, M., Karniadakis, G.E., and Kelley, D.H. (2023). Artificial intelligence velocimetry reveals in vivo flow rates, pressure gradients, and shear stresses in murine perivascular flows. Proc. Natl. Acad. Sci. USA *120*, e2217744120.
43. Ray, L.A., and Heys, J.J. (2019). Fluid Flow and Mass Transport in Brain Tissue. Fluid *4*, 196.
44. Damkier, H.H., Brown, P.D., and Praetorius, J. (2013). Cerebrospinal Fluid Secretion by the Choroid Plexus. Physiol. Rev. *93*, 1847–1892.
45. Sokoloff, L. (2004). Energy metabolism in neural tissues in vivo at rest and in functionally altered states. In Brain Energetics and Neuronal Activity: Applications to fMRI and Medicine, R.G. Shulman and D.L. Rothman, eds. (Wiley).

46. Williamson, N.H., Komlosh, M.E., Benjamini, D., and Basser, P.J. (2020). Limits to flow detection in phase contrast MRI. J. Magn. Reson. Open *2–3*, 100004.

47. Magdoom, K.N., Zeinomar, A., Lonser, R.R., Sarntinoranont, M., and Mareci, T.H. (2019). Phase contrast MRI of creeping flows using stimulated echo. J. Magn. Reson. *299*, 49–58.

48. Almudayni, A., Alharbi, M., Chowdhury, A., Ince, J., Alablani, F., Minhas, J.S., Lecchini-Visintini, A., and Chung, E.M.L. (2023). Magnetic resonance imaging of the pulsing brain: a systematic review. Magn. Reson. Mater. Phys., Biol. Med. *36*, 3–14.

49. Bayer, T.A. (2015). Proteinopathies, a core concept for understanding and ultimately treating degenerative disorders? Eur. Neuropsychopharmacol. *25*, 713–724.

50. Szentistvanyi, I., Patlak, C.S., Ellis, R.A., and Cserr, H.F. (1984). Drainage of interstitial fluid from different regions of rat brain. Am J Physiol-renal *246*, F835–F844.

51. Lilius, T.O., Rosenholm, M., Klinger, L., Mortensen, K.N., Sigurdsson, B., Mogensen, F.L.H., Hauglund, N.L., Nielsen, M.S.N., Rantamäki, T., and Nedergaard, M. (2022). SPECT/CT imaging reveals CNS-wide modulation of glymphatic cerebrospinal fluid flow by systemic hypertonic saline. iScience *25*, 105250.

52. Giannetto, M., Xia, M., Stæger, F.F., Metcalfe, T., Vinitsky, H.S., Dang, J.A.M.L., Xavier, A.L.R., Kress, B.T., Nedergaard, M., and Hablitz, L.M. (2020). Biological sex does not predict glymphatic influx in healthy young, middle aged or old mice. Sci. Rep. *10*, 16073.

53. Xavier, A.L.R., Hauglund, N.L., von Holstein-Rathlou, S., Li, Q., Sanggaard, S., Lou, N., Lundgaard, I., and Nedergaard, M. (2018). Cannula Implantation into the Cisterna Magna of Rodents. J. Vis. Exp. *135*, 57378. https://doi.org/10.3791/57378.

54. Ghali, M.G.Z. (2018). Microsurgical technique for tracheostomy in the rat. MethodsX *5*, 61–67.

55. Varga-Szemes, A., Kiss, P., Rab, A., Suranyi, P., Lenkey, Z., Simor, T., Bryant, R.G., and Elgavish, G.A. (2016). In Vitro Longitudinal Relaxivity Profile of Gd(ABE-DTTA), an Investigational Magnetic Resonance Imaging Contrast Agent. PLoS One *11*, e0149260.

56. Tustison, N.J., Avants, B.B., Cook, P.A., Zheng, Y., Egan, A., Yushkevich, P.A., and Gee, J.C. (2010). N4ITK: Improved N3 Bias Correction. Ieee T Med Imaging *29*, 1310–1320.

STAR★METHODS

KEY RESOURCES TABLE

REAGENT or RESOURCE	SOURCE	IDENTIFIER
Chemicals, peptides, and recombinant proteins		
Sodium chloride	Sigma-Aldrich	S3014; CAS: 7647-14-5
Ketamine	MSD	Ketaminol Vet 100 mg/mL
Dexmedetomidine	Orion Pharma	Dexdomitor 0.5 mg/mL
Lidocaine	Accord	Lidocain Accord 10 mg/mL
Carprofen	Zoetis	Rimadyl 50 mg/mL
Gado-DTPA	BioPal	Gadolinium-DTPA 469 mg/ml
Gadospin P	Viscover	Cat# 130-095-136
Ketamine	MSD	Ketaminol Vet 100 mg/mL
Dexmedetomidine	Orion Pharma	Dexdomitor 0.5 mg/mL
Lidocaine	Accord	Lidocain Accord 10 mg/mL
Carprofen	Zoetis	Rimadyl 50 mg/mL
Gado-DTPA	BioPal	Gadolinium-DTPA 469 mg/ml
Gadospin P	Viscover	Cat# 130-095-136
Deposited data		
Unprocessed MRI data and code for Figures 1, 2, 3, and 5	This paper	https://doi.org/10.17632/78rvmj2wh8.1
Experimental models: Organisms/strains		
Rat: Sprague-Dawley	Janvier	Sprague-Dawley rats
Software and algorithms		
ITK-SNAP v4.2.0	itksnap.org	RRID:SCR_002010
GraphPad Prism v9.2.0	graphpad.com	RRID:SCR_002798
Matlab R2023b	mathworks.com/products/matlab/	RRID:SCR_001622
ANTs - Advanced Normalization Tools v2.3.4	github.com/ANTsX	RRID:SCR_004757
Python Programming Language v3.11.6	python.org	RRID:SCR_008394
FSL 6.0.7.4	fmrib.ox.ac.uk/fsl/	RRID:SCR_002823
MRIcroGL v1.2.20201102	nitrc.org/projects/mricrogl	RRID:SCR_024413
GraphPad Prism v9.2.0	graphpad.com	RRID:SCR_002798
Matlab R2023b	mathworks.com/products/matlab/	RRID:SCR_001622
ANTs - Advanced Normalization Tools v2.3.4	github.com/ANTsX	RRID:SCR_004757
Python Programming Language v3.11.6	python.org	RRID:SCR_008394
FSL 6.0.7.4	fmrib.ox.ac.uk/fsl/	RRID:SCR_002823
MRIcroGL v1.2.20201102	nitrc.org/projects/mricrogl	RRID:SCR_024413

EXPERIMENTAL MODEL AND STUDY PARTICIPANTS DETAILS

A total of 33 Sprague-Dawley rats (175-400 g) were included in the study, all acquired from Janvier (Le Genest-Saint-Isle, France) of which 8 served as the control group for another study.[51] Since biological sex does not appear to affect glymphatic inflow,[52] we used a mix of male and female rats (12 male, 21 female). Rats were housed in 12:12 light cycle in individually ventilated cages with *ad libitum* access to food and water. All housing, treatments and imaging were performed according to protocols approved by the Danish Animal Experiments Inspectorate (approval number 2015-15-0201-00535).

METHOD DETAILS

Cisterna magna cannulation

The rats were anesthetized with a mixture of ketamine (100 mg/kg, Ketaminol® Vet, MSD) and dexmedetomidine (0.5 mg/kg, Dexdomitor, Orion Pharma, Espoo, Finland) administered subcutaneously (2 ml/kg). After a loss of toe-pinch reflex, the animals were fixed to a stereotaxic frame with head tilted slightly forward (30°). The cannula was inserted to cisterna magna (CM) as previously described, with minor modifications.[53] Briefly, the atlanto-occipital membrane overlying the CM was surgically exposed and a cannula consisting of a 30G short-beveled dental needle attached to PE10 tubing was carefully inserted into the intrathecal space while avoiding any CSF leak outside CM. The cannula was fixed to the dura with cyanoacrylate glue and dental cement.

Mechanical ventilation

For mechanical ventilation, the rats were tracheotomized under ketamine/dexmedetomidine anesthesia (100 mg/kg+0.5 mg/kg, s.c.). A tracheal cannula was inserted essentially as described previously with minor modifications.[54] A ventral midline cervical incision was made from the manubrium sterni to the level of hyoid bone. Trachea was exposed by lateral retraction of sternohyoid muscles overlaying the trachea. A 3-0 silk suture was placed underneath the trachea and a cut was made through the upper half of the trachea with iridectomy scissors caudally to the suture. A cannula was placed in the trachea and secured with the pre-placed suture. The cervical incision was sutured tightly with 3-0 silk suture. The cannula was connected to MRI-1 small animal ventilator (CWE Inc., Ardmore, PA, USA) and microCapStar End-Tidal CO_2 Analyzer (CWE Inc., Ardmore, PA, USA). Rats were ventilated with 60/40% mixture of N_2/O_2 using a respiration rate of 75 min^{-1}. Inspiration volume was adjusted between 1.2–1.6ml to achieve $EtCO_2$ of 35–40 mmHg.

MRI experiments

MRI experiments were carried out on a 9.4T magnet Bruker BioSpec 94/30 USR) interfaced to a Bruker Avance III console and controlled by Paravision software (Bruker) v5. Imaging was carried out using an 86 mm volume RF-transmit coil and a 4-channel phased array RF receiver coil (Bruker). Rats were placed prone in the magnet with the teeth fixed in a bite bar. The surface receiver coil was centered over the cerebrum. Core temperature and respiration (in the case of non-ventilated experiments) were monitored using an MRI-compatible monitoring system (SA Instruments) for the duration of the experiment and heated waterbed was used to maintain the core temperature at 36.5°C–37.5°C.

Imaging consisted of anatomical T2-weighted Rapid Acquisition with Relaxation Enhancement (RARE) images (echo time (TE): 36 ms, repetition time (TR): 16 s, RARE factor: 8, matrix: 330x384, FOV: 30x35 mm,128 slices, slice thickness: 0.312 mm; slice overlap: 0.156 mm, 2 frames) followed by quantitative DCE-MRI acquired using the same sequence as described previously.[21,23] Briefly, quantitative DCE-MRI imaging consisted of a double angle-experiment to measure RF transmission inhomogeneity using the 2D RARE sequence (TE: 22 ms, TR: 10 s, RARE factor: 4, 50 slices, matrix 128x128, FOV: 30x32mm, slice thickness: 0.4 mm; slice gap: 0.2 mm; flip angle (FA): 70° and 140°), followed by variable flip angle SPGR to measure a baseline T1-map (TE: 4 ms, TR: 15 ms, matrix: 128x128x128, FOV: 30x32x30, FA: 2, 5, 10, 15, 20, 30, frame rate: 4m5s min) and DCE-MRI for the GadospinP experiment consisted of 3D SPGR images map (TE: 4 ms, TR: 15 ms, matrix: 128x128x128, FOV: 30x32x30 mm, flip angle (FA): 15, frame rate: 4m5s min, 3 baseline frames, 42 post-infusion frames). Gd-DTPA concentration was the quantified as previously described for Gd-DOTA,[21] using a longitudinal relativity constant for GD-DTPA[55] at 9.4 T and 37°C of 2.94 $s^{-1}mM^{-1}$. For GadospinP experiments, only DCE-MRI was acquired, consisting of 3D SPGR images map (TE: 2.2 ms, TR: 11.6 ms, matrix: 280x75x340, FOV: 28x15x34 mm, FA: 15, frame rate: 2m30s min, 3 baseline frames, 24 post-infusion frames).

We validated PVS cross-sectional area MRI using high-resolution T2-weighted anatomical MRI from 12 rats (7 male). The rats served as control subjects for a different study for which 5 were mechanically ventilated, 7 breathed spontaneously. Imaging consisted of high resolution T2-weighted images (TE: 24.1ms, TR: 16s, Echo spacing: 8.033, RARE factor: 8, matrix: 375x250, field of view (FOV): 30x20mm, 128 slices, 220um slice thickness, 110 um overlap, 8 repetitions, frame rate 6m8s). These data also served as the basis for the population-based MRI template.

PVS distance measurements

To measure distances in the curved path of the perivascular space, we first created a graph $G = (V,E)$, where vertices V were voxels included in a given region of interest (ROI) and E were edges between neighboring voxels (26-connectivity) with weights corresponding to the Euclidian distance between the voxel centers. Then, for each pixel in the ROI, we calculated a shortest-path distance to the root, which was a manually designated starting voxel at the bottom of the middle cerebral artery.

PVS cross-sectional area estimation

Due to the small size of the perivascular spaces compared to imaging resolution, the cross-sectional area of the perivascular space could not be measured directly but was instead measured as the PVS volume of an 8 mm proximal segment of the MCA divided by its length. CSF volume fraction maps were produced as follows: T2-weighted TurboRARE images were rigidly motion corrected and averaged, and bias field corrected by (1) in-house software to remove a second-order bias field in the ventral-dorsal direction due to the use of a surface receiver coil and (2) N4[56] to remove local bias fields. As T2 of CSF is much higher than in tissue, we assumed that the bias corrected signal difference between CSF and brain parenchyma to be approximately proportional to the CSF volume

fraction in a voxel. CSF volume fraction maps were calculated by setting mean cortical image intensity near the MCA as 0% CSF and average image intensity centrally in the basal cistern, where CSF width exceeded 3 voxels, as 100% CSF.

Bilateral ROIs were drawn using ITK-SNAP (v3.8.0) to include the perivascular spaces around MCA. Total PVS volume was calculated as the sum of all CSF volume fractions in the ROI multiplied by the per-voxel volume, and average cross-sectional area was calculated as the ratio between the volume and length of the PVS segment.

Velocity estimation

DCE-MRI images were concatenated and motion corrected. Perivascular space flow velocity was estimated in 8 mm proximal segments of the middle cerebral artery in both hemispheres. Bilateral ROIs were drawn using ITK-SNAP (v3.8.0) to include the perivascular spaces around MCA. A distance map was then computed as described above using the voxel closest to the circle of Willis as starting voxel. Distances were binned in segments of 1 mm and time-concentration curves were summed for each bin. Time-concentration curves were resampled at 10 times the imaging frame rate and time-of-arrival was then calculated as the first time point at which tracer concentration exceeded 20% of maximum. Finally, we fitted a first-degree polynomial to the time-of-arrival vs. distance plot to calculate velocity (Figure 2D).

MCA CSF perfusion volume estimation

4D (xyz + time) DCE-MRI-images were concatenated, motion corrected, and smoothed in the time dimension by applying a moving average filter with a window of 3 frames. For each voxel $p = (x, y, z)$ within the brain, time-signal-curves, $S(p,t)$, were used to calculate the time of tracer arrival. We denote the first time-point at which $S(p,t) > \max_t (S(p)) \cdot 0.2$ as t_1, and the preceding time-point t_0. Arrival time was then found as the intercept with the x-axis, i.e.

$$t_a(p) = t_0 - S(p,t_0)\frac{t_1 - t_0}{S(p,t_1) - S(p,t_0)}$$

resulting in the per-voxel map of tracer arrival time, $t_a(p)$ (Figure 3C).

CSF probability maps were calculated as described above, and a threshold of CSF probability of 0.1 was used to create a CSF segmentation. Using the in-house T2-weighted TurboRARE average template,[25] a segmentation of the territories of the left and right MCA in the pial surface was drawn manually. This segmentation was then transformed to the individual rat data.

A gradient ascent algorithm was then used to trace the source of glymphatic perfusion to each voxel in the parenchyma. Starting from each voxel (p_0) in the brain parenchyma, the algorithm iteratively stepped 0.2 mm in the opposite direction to the gradient of the tracer arrival time map, i.e.

$$p_{i+1} = p_i - \frac{\nabla t_a(p_i)}{|\nabla t_a(p_i)|} \cdot 0.2 \text{ mm},$$

where ∇ is the gradient operator and $|\cdot|$ is the Euclidian norm. Stepping stopped when

- p_{i+1} contained MCA perivascular space; Territory(p_0) was then assigned the value of the influx route map at p_{i+1},
- p_{i+1} was outside the brain; Territory(p_0) was then assigned the value of 0, or
- $(i + 1) \cdot 0.2\,mm > 20\,mm$; Territory$(p_0)$ was then assigned the value of 0.

Finally, holes in the Territory map were filled using the morphological image close operation.

SPECT imaging

We used dynamic SPECT/CT imaging after intrastriatal injection to measure the brain efflux rate. These experiments also served as the control group in a different study.[51] An intrastriatal cannula was surgically placed on the day before imaging. The rats were anesthetized with isoflurane (3.5-4% induction, 1.5-2% maintenance in O_2, Attane Vet, ScanVet). After a loss of toe-pinch reflex, the animals were placed on a heating pad and fixed to a stereotaxic frame. Prior to the surgery, the rats received systemic carprofen (5 mg/kg, s.c. Rimadyl Bovis Vet, Zoetis) and local infiltration anesthesia with lidocaine (1 mg/kg, s.c. Accord Healthcare Ltd.) locally at the surgical site. The skull was surgically exposed, and a small burr hole was drilled to the skull above the striatum (M/L: 3.0 mm; A/P: 0.0 mm). A guide cannula was placed through the burr hole (D/V: +5.0 mm) and fixed to the skull with dental cement and cyanoacrylate glue. The rats were allowed to recover for 16-24 h in single-housing before SPECT/CT imaging. For the duration of the scans, rats were anesthetized with a mixture of ketamine (100 mg/kg) and dexmedetomidine (0.5 mg/kg) administered subcutaneously (2 ml/kg). The respiratory rate was monitored with a pressure pad to ensure sufficient level of anesthesia. No supplemental anesthesia was needed in any of the scans. Dynamic whole-body SPECT/CT imaging was performed with the Vector4CT (MILabs, Utrecht, Netherlands) system. Rats were placed in the scanner in prone position. SPECT images were acquired with a high energy ultra-high-resolution rat 1.8 mm pinhole collimator (HE-UHR-RM 1.8 mm pinhole). The rectal temperature of the animal was monitored throughout the whole scan and normothermia was maintained with a heating pad. ^{99m}Tc-labeled diethylenetriaminepentaacetic acid (12.5 mg/ml, TechneScan DTPA, Curium Pharma, The Netherlands) with a molecular weight of 489 Da was infused over the first 20 minutes (0.2 μl/min, 3–7 MBq) of scan with a Hamilton Gastight 1700 syringe (Bonaduz, Switzerland) in a micro infusion pump.

Image data were acquired over 3 h 40 min (twenty-two 10-minute scans). The SPECT image was registered to full-body CT images acquired directly after the SPECT scans in the same imaging sessions that served as anatomical reference images.

SPECT/CT analysis

Acquired images were reconstructed using Similarity-Regulated Ordered Subsets Estimation Maximization (SROSEM) with a voxel size of 300 μm and 5 iterations and corrected for attenuation and tracer decay in MILabs Reconstruction software 10.16 (MILabs, Utrecht, Netherlands). Intracranial region of interest (ROI) was defined in ITK-SNAP software with automated segmentation using the acquired SPECT and CT images. The total injected radioactivity was calculated in the whole animal and urine pad (excluding residual activity in the infusion cannula) in the first frame after the end of tracer infusion. The fraction of the total activity in the injected dose (%ID) in intracranial ROI was calculated from the acquired SPECT images using MATLAB.

QUANTIFICATION AND STATISTICAL ANALYSIS

All image registration was performed using Advanced Normalization Tools Advanced Normalization Tools (ANTs). Image processing was performed in MATLAB R2019B, Python v.3.8.3, or the FMRIB Software Library v. 6.0. MRI volume rendering was carried out in MRIcroGL v1.2.20201102. Statistical analysis consisted of paired and unpaired t-tests, and linear regression and was carried out in GraphPad Prism v. 9.2.0. All measurements are reported as mean ± standard deviation and error bars represent standard deviation. n represent biological replicates, i.e. number of rats. Unless otherwise noted, in the case of measurements calculated for each hemisphere separately (i.e. $|\vec{v}_{PVS}|$, A_{PVS}, $m_{territory}$, and Q_{in}), each biological replicate was represented by the average of the two per-hemisphere measurements. *: $p < 0.05$, *** $p < 0.001$, **** $p < 0.0001$.